Article

Photocorrosion of Hematite Photoanodes in Neutral and Alkaline Electrolytes

Victoria Benavente Llorente,* Ken J. Jenewein, Markus Bierling, Andreas Körner, Andreas Hutzler, Attila Kormányos,* and Serhiy Cherevko*

Read Online

ACCESS | 📊 Metrics & More | 📖 Article Recommendations | 🆂🅸 Supporting Information

ABSTRACT: Photoelectrochemical (PEC) water splitting is a promising energy conversion technology based on the harvesting of sunlight to produce green hydrogen. One of the major challenges hindering the development of PEC devices is the stability of photoanodes since most semiconductors are susceptible to anodic decomposition in aqueous solutions. While hematite (α-Fe$_2$O$_3$) has been regarded as one of the most stable metal oxides to drive the oxygen evolution reaction in alkaline media, its photostability in a broad pH range is poorly investigated. In this work, we study the dissolution of model Fe$_2$O$_3$ thin films in different electrolytes, including unbuffered and buffered neutral, near-neutral, and alkaline solutions, using on-line PEC inductively coupled plasma mass spectrometry. Fe leaching is observed in all studied unbuffered electrolytes under irradiation while phosphate-buffered electrolytes reveal a dramatic stability enhancement at all pHs. The latter might imply that phosphate buffers either alleviate local acidification in the close vicinity of the electrode−electrolyte interface during the reaction or that specific adsorption of phosphate anions at the α-Fe$_2$O$_3$ surface could mitigate dissolution. Furthermore, we explore the long-term stability of α-Fe$_2$O$_3$ using a three-electrode bulk PEC cell. In the long run, phosphate buffers do not represent an optimal electrolyte choice either, as the surface Fe oxide gradually converts to Fe phosphates that are not photoelectrochemically active. Our work demonstrates that photocorrosion of Fe$_2$O$_3$ within electrolytes that are commonly used in the literature is not negligible and should be considered for designing stable semiconductor interfaces.
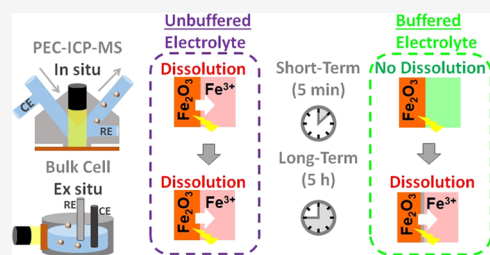
1. INTRODUCTION

The depletion of fossil fuels and the global climate crisis have made it imperative to harvest renewable energy sources. Therefore, transforming solar energy directly into chemical bonds has drawn great attention in the scientific community as a sustainable solution for energy storage.[1−3] Photoelectrochemical (PEC) cells directly use the energy of sunlight to produce energy-dense fuels, e.g., green hydrogen. In typical PEC cells, n-type semiconductors are used as photoanodes to drive the oxygen evolution reaction (OER). P-type semiconductors are applied as the photocathode where, depending on applications, the hydrogen evolution reaction (HER) and/ or carbon dioxide reduction reaction (CO$_2$RR) or other cathodic reactions take place.

One of the longstanding challenges in PEC water splitting is finding semiconductor photoanode materials that can withstand the harsh OER conditions in broad potential and pH ranges.[3,4] Photoanodes based on metal oxide materials, such as ZnO, TiO$_2$, WO$_3$, BiVO$_4$, or α-Fe$_2$O$_3$ (herein denoted as Fe$_2$O$_3$), have been extensively studied due to their natural abundance, low cost, and high PEC water splitting activity, as well as their chemical stability.[5−8] However, the lifetime of PEC devices containing these semiconductors is usually in the range of hours or several days,[9−11] still far apart from what is required for practical applications. Indeed, a techno-econom-

ical analysis has set a lifetime of at least 7−10 years for a solar module to be economically feasible.[12] It is obvious that on the way toward stabilizing PEC devices (either through optimizing materials or operational conditions), fundamental research on the mechanisms of degradation processes, for example, photocorrosion, is indispensable.

Photocorrosion is a degradation process that takes place when photogenerated charge carriers participate in the self-oxidation or self-reduction of the semiconductor photoelectrode rather than driving the desired redox reactions, e.g., OER and HER. Gerischer et al. defined the thermodynamic stability criteria for different semiconductor materials immersed in aqueous electrolytes.[13−15] A photoanode is stable against anodic photocorrosion if the self-oxidation potential is more positive (relative to the standard hydrogen electrode (SHE)) than the O$_2$/H$_2$O redox potential or the valence band maximum. However, thermodynamic schemes only indicate the spontaneity of the reactions. Competition between the
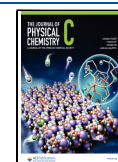
OER and self-oxidation is highly influenced by the kinetic parameters of both the OER and photocorrosion.

Out of the most promising oxides, Fe_2O_3 has been extensively studied as a metal oxide photoanode for the PEC OER due to its narrow band gap (1.9–2.2 eV), appropriate conduction band position for water oxidation, abundance, and nontoxicity. Nevertheless, Fe_2O_3 has inherent disadvantages, such as short-hole diffusion length (2–4 nm) and poor conductivity, hindering the transport of holes toward the interface to oxidize water.[16,17] To tackle these, nanostructuring and doping were adopted as strategies to improve the PEC performance.[18−20] Less has been done with regard to the photostability of Fe_2O_3-based photoanodes in different electrolytes. While alkaline, neutral, and near-neutral electrolytes are typically considered,[21−28] linking the pH shift in near-neutral electrolytes to *in situ* Fe_2O_3 dissolution was recently demonstrated.[29] The stability of Fe_2O_3 photoanodes modified with Ir molecular catalysts (Fe_2O_3 + Ir MC) was studied in unbuffered solutions at different pH values using on-line mass spectrometry in a newly published work.[29] Fe_2O_3 was the least stable under near-neutral conditions (pH 5.7), mainly due to local pH shifts as a result of generating H^+ during the OER. The work highlighted that pH is a crucial parameter for the activity–stability of the Fe_2O_3 + Ir MC system, calling for a more detailed study of the stability of bare Fe_2O_3 photoanodes in different pHs and electrolytes. Several works have revealed the increased photocorrosion of Fe_2O_3 in acidic electrolytes.[22,30−34] However, detailed information about the rates of Fe dissolution and its dependence on the electrolyte species and pH is still missing. This knowledge is of relevance since Fe_2O_3 has been used to construct photoanodes to drive the PEC water splitting in mild conditions (neutral electrolytes).[35−39] Recently, coupling on-line inductively coupled plasma mass spectrometry (ICP-MS) to PEC measurements has provided novel insights into the light-triggered photodegradation of WO_3, $BiVO_4$, and TiO_2 photoanodes,[40−43] proving to be an excellent approach to reveal different degradation pathways.

In this work, we systematically investigate the photocorrosion of nanostructured Fe_2O_3 model thin film photoanodes in neutral, near-neutral, and alkaline electrolyte solutions by using different buffered and unbuffered solutions. To assess the stability quantitatively, we use a photoelectrochemical scanning flow cell (PEC-SFC) coupled to on-line ICP-MS (PEC-ICP-MS) to detect metal dissolution during the OER. Moreover, we performed long-term measurements in a bulk cell using the same buffered and unbuffered electrolytes to contrast with the results obtained with the PEC-ICP-MS setup and gain insight into degradation processes occurring at different time scales. We demonstrate that photocorrosion of Fe_2O_3 highly depends on the nature of the electrolyte, the pH, and the time scale of the experiment.

2. MATERIALS AND METHODS

2.1. Synthesis of Hematite Nanorods.
Fe_2O_3 nanorods were synthesized on a fluorine-doped tin oxide (FTO) glass substrate (TEC15, Sigma-Aldrich) using an adapted hydrothermal method. In a typical experiment, a piece of cleaned FTO (2.5 cm × 2.5 cm) was immersed in 15 mL of aqueous solution containing 0.1 M $FeCl_3 \cdot 6H_2O$ (≥99%, Sigma-Aldrich), 0.1 M $NaNO_3$ (≥99.0%, Sigma-Aldrich), and 15 μL of concentrated HCl 34%. The reaction was conducted using a 50 mL Teflon-lined reactor at 100 °C in a convection

oven for 2 h. The obtained uniform FeOOH film was thoroughly rinsed and ultrasonicated with deionized water to detach any loosely adsorbed nanoparticles. The substrates were annealed on air sintered at 550 °C for 3 h to transform the FeOOH films into Fe_2O_3 and further sintered for 10 min at 800 °C.

2.2. Optical and Morphological Characterization.
Visible absorption spectra were acquired using an optical spectrophotometer (OceanOptics) equipped with a deuterium−halogen light source (DH-2000-L) and an HR4000 spectrometer.

The structure of the synthesized Fe_2O_3 thin film was investigated by scanning electron microscopy (SEM). The imaging was conducted using a Zeiss Crossbeam 540 focused ion beam scanning electron microscope (FIB-SEM) with a Gemini II column (Carl Zeiss AG) applying an accelerating voltage of 3 kV. The FTO glass substrates were attached to aluminum SEM specimen stubs with a double-sided adhesive copper tape for surface imaging. For cross-sectional imaging, the sample was fractured along a breaking edge received by a diamond scriber. Afterward, the sample was fixed vertically on an SEM-slotted specimen stub. The conductivity of the samples was improved by gold sputter coating (108 Manual Sputter Coater, Cressington) and using a conductive silver tape.

High-resolution scanning transmission electron microscopy (HR-STEM) was performed using a Talos F200i instrument from Thermo Fisher Scientific operated at an accelerating voltage of 200 kV. The microscope features an X-FEG and a Dual Bruker XFlash 6|100 energy dispersive spectroscopy (EDS) detector. The beam current was set to 240 pA, and a high-angle annular dark field (HAADF) detector was used for imaging.

2.3. PEC-ICP-MS Measurements.
Photoelectrochemical measurements were carried out with an experimental setup reported previously.[44] An electrochemical scanning flow cell (SFC) made from polytetrafluoroethylene was coupled to the counter electrode (graphite rod), the reference electrode (Metrohm Ag/AgCl, 3 M KCl), and an inductively coupled plasma mass spectrometer (ICP-MS; PerkinElmer NexION 300) by Tygon tubing. The working electrode was fixed on a movable, LabView-controlled XYZ stage (Physical Instruments), making contact with the SFC opening (0.059 cm^2 area). The working electrode was contacted with a copper tape. Electrochemical measurements were controlled with a Gamry Rerence 600 potentiostat. Measured potentials were converted to the reversible hydrogen electrode (RHE) by using the following equation: $E_{RHE} = E_{Ag|AgCl} + 0.197$ V + 0.059 pH.

The optical arrangement of PEC-ICP-MS was described previously.[44] In brief, the light was emitted from a 300 W ozone-free Xe lamp (Newport), passed through an AM 1.5G filter (Newport), and channeled into the PEC-SFC via a liquid light guide (Newport). The light intensity at the opening of the SFC was adjusted to 100 mW cm^{-2} every day prior to measurements, using a calibrated photovoltaic cell normalized to an illumination area of 0.059 cm^2. Electrolytes were prepared fresh every day. The unbuffered solutions were prepared as follows: 50 mM $NaClO_4$ (Acros Organics) was used as a neutral electrolyte, 50 mM $NaClO_4$ with the addition of small aliquots of concentrated $NaOH \cdot H_2O$ (99.99% suprapur, Merck) was used as a near-neutral electrolyte, and 50 mM NaOH was used as an alkaline electrolyte. The

buffered electrolytes were prepared according to the following description: a solution of 25 mM K_2HPO_4 (99.995% suprapur, Merck) and 25 mM KH_2PO_4 (99.995% suprapur, Merck) served as a neutral electrolyte, 50 mM K_2HPO_4 was used as a near-neutral electrolyte, and a solution based in 50 mM K_2HPO_4 and 25 mM NaOH was used as an alkaline solution. All solutions were prepared with deionized (DI) water (Merck, Milli-Q). The pH value of all solutions was controlled before the experiments. The electrolyte reservoir was continuously purged with Ar (5.0, AirLiquide).

ICP-MS was calibrated every day for Fe with freshly prepared standards (Merck Certipur) in the respective electrolyte with a four-point calibration (0; 0.5; 1.0; 5.0 μg L^{-1}). A Co solution of 10 μg L^{-1} concentration served as the internal standard. To avoid the $^{40}Ar^{16}O^+$ interference with $^{56}Fe^+$, a dynamic reaction cell was used, with a methane gas flow of 0.8 mL min^{-1}.

2.4. Bulk-Cell Measurements. The long-term measurements were performed using a commercial PEC three-electrode cell (PEC 15 × 15 mm², redox.me), formed by a Ag|AgCl reference electrode and a graphite rod as the counter electrode. The light source was provided by the same optical arrangement used in PEC-ICP-MS, using a liquid light guide to irradiate the working electrode from the back (0.5 cm²). The electrolyte was purged with Ar (5.0, AirLiquide) 15 min prior to each measurement, and an Ar flux was maintained through the gas inlet/outlet of the bulk cell during the measurement.

3. RESULTS AND DISCUSSION

3.1. Synthesis and Characterization of Nanostructured Fe2O3. Conclusions in our study are valid only if the photocorrosion measurements are performed on ideal model systems that bear similar morphology, electronic properties, and PEC activity to the Fe_2O_3 photoelectrodes reported in the literature. Therefore, uniform nanostructured Fe_2O_3 films were prepared using a hydrothermal method and a two-step annealing protocol.[45] In this work, a first annealing step of 3 h at 550 °C was performed to convert the FeOOH obtained from a hydrothermal deposition method to Fe_2O_3. A second annealing step of 10 min at 800 °C was included to activate the samples.[46] All of the characterizations and results presented in this work correspond to hematite photoanodes prepared with the two-step annealing protocol.

The morphology and thickness of the Fe_2O_3 thin films were characterized by scanning electron microscopy (SEM). Figure 1a shows that the prepared photoanode consists of uniformly distributed nanorods with diameters of ca. 70 nm. The cross-sectional view (see Figure 1b) reveals that vertically aligned nanorods were obtained, with lengths in the order of 200 nm. The optical properties of the film were characterized using ultraviolet–visible (UV–vis) absorption spectroscopy. The optical band gap was estimated from a Tauc plot (see Figure 1c) using the UV–vis spectrum, shown in Figure S1 in the electronic Supporting Information (SI).[47] The determined band gap of 2.06 eV is in good agreement with the indirect band gap values found in the literature for Fe_2O_3 nanorods.[48,49] The crystal structure of the prepared nanorods was characterized using selected area electron diffraction (SAED) (Figure S2a). The theoretical model of Fe_2O_3 powder diffraction indicated with red lines agrees well with the measured SAED pattern indicating the phase of Fe_2O_3 to be mainly hematite (α-Fe_2O_3). Further, measured lattice plane distances, as shown in Figure S2b, are also in good agreement
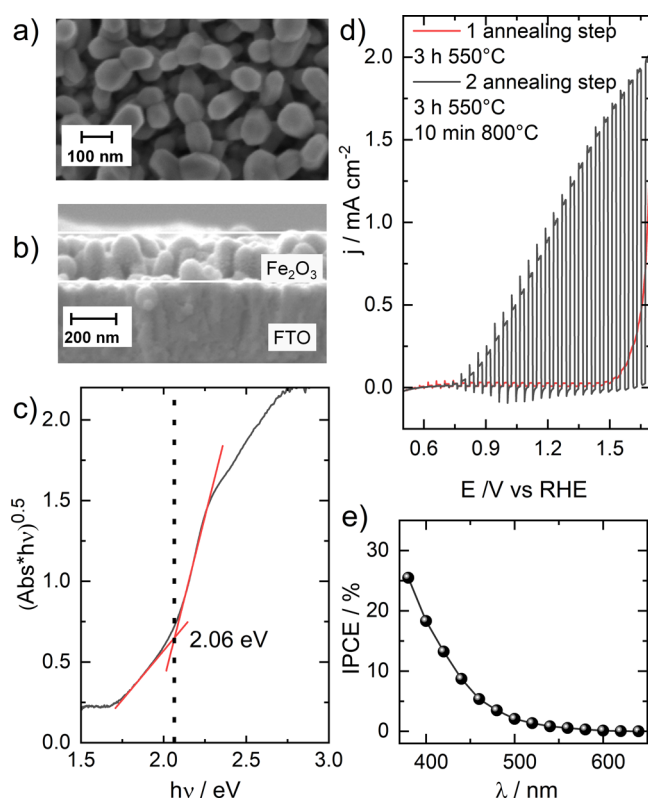

Figure 1. Characterization of the synthesized Fe_2O_3 thin film. SEM images: (a) top view and (b) cross-sectional view. (c) Tauc plot obtained from the UV–vis spectrum. (d) Chopped linear sweep voltammetry under irradiation with different annealing protocols recorded at a scan rate of 10 mV s^{-1}. (e) Incident photon to current efficiencies at 1.23 V_{RHE}. All PEC measurements presented in this figure were conducted in a 50 mM NaOH solution.

with the theoretical model using the lattice parameters of Fe_2O_3.[50]

Pristine Fe_2O_3 nanorods typically have low incident photon to current efficiency (IPCE) values when no elemental dopants are added or low annealing temperatures are used.[51−53] The PEC performance of the vertically aligned nanorods was characterized using the photoelectrochemical scanning flow cell (PEC-SFC) setup.[44] As can be observed in Figure 1d, the two-step annealing remarkably improves the obtained photocurrent. The diffusion of Sn^{4+} from the tin oxide substrate into the Fe_2O_3 nanostructures was reported for annealing temperatures above 650 °C.[54] Therefore, at 800 °C, Sn^{4+} impurities could incorporate into the Fe_2O_3 lattice as dopants, improving the photoelectrochemical properties of the photoanode. To corroborate if Sn diffused into the nanorods during the two-step annealing, the composition of Fe_2O_3 was analyzed using STEM energy dispersive X-ray spectroscopy (EDXS), and we observed indeed the presence of Sn (0.5 atom %) homogeneously distributed along the nanorod structure. The IPCE was measured at different wavelengths using monochromatic light in the alkaline electrolyte. The results are presented in Figure 1e, showing that the obtained IPCEs are in the range of state-of-the-art values found in the literature for Fe_2O_3 nanorods (e.g., ~16% at λ = 400 nm).[54,55] In summary, the hydrothermal method used in this work was successful in obtaining Fe_2O_3 nanorods with optical, morphological, and PEC properties comparable to those reported in the literature.

3.2. Photoactivity and Stability of the Fe_2O_3 Films in Different Electrolytes and pHs. After ensuring that the thin films possess the desired physicochemical properties, their photoactivity and photostability were systematically characterized in:

(a) unbuffered alkaline (pH = 12.7), near-neutral (pH = 9.5), and neutral (pH = 6.4) solutions;
(b) buffered alkaline (pH = 11.7), near-neutral (pH = 9.5), and neutral (pH = 7.0) solutions.

The selected pHs are the most commonly used to characterize Fe_2O_3 photoanodes.[22−26,56,57] Unlike the majority of previous reports of PEC-ICP-MS measurements using light-emitting diodes with an irradiance output different from the solar irradiance spectrum,[40−42,58−60] this setup allows studying the photocorrosion phenomena under realistic irradiation conditions (AM 1.5G 100 mW cm^{-2} light intensity) that match well with the ones used widely in the PEC literature.[29,44,61]

To estimate the effect of illumination on the activity, two cyclic voltammograms (CVs) were recorded consecutively: one in the dark and one under irradiation, applying a scan rate of 10 mV s^{-1}. The measured currents for the unbuffered and buffered solutions are shown in Figure 2. Dark currents are negligible in all of the solutions. Upon irradiation, a photocurrent is observed with different values and the onset

potential of photocurrent (defined as the potential at which the photocurrent value reaches 10 μA cm^{-2}) depends on the pH of the electrolyte (see Table S1). The trends found for the illuminated CVs show that the onset potential shifts cathodically and the obtained photocurrent is higher when the pH is increased for unbuffered and buffered electrolytes.

The photocurrent enhancement at higher pHs is well known in the literature and was demonstrated for unbuffered[62−64] and buffered solutions.[65] As for the dependence of the photocurrent onset potential on pH, Iandolo et al. reported a quasi-Nernstian behavior.[62] At the same time, other groups have found two pH ranges with different dependencies on pH.[63,65] This pH-dependent performance has been ascribed to an interplay between (a) the semiconductor surface energetics and (b) the interfacial reaction kinetics during the OER.[65] Singly coordinated oxygen sites on the surface of Fe_2O_3 ($Fe^{III}−OH$) can uptake and release protons ($pK_a \sim 10$),[66,67] leading to the dependence of the interfacial properties on the pH value of the electrolyte.

Regarding the kinetics aspects, Liu et al.[65] suggested that below pH 10, the change in the OER mechanism leads to a surface accumulation of charge carriers,[63,64] causing Fermi Level Pinning (FLP). The FLP ultimately rules the obtained photocurrents and shifts the photocurrent onset. Although the CVs recorded in buffered solutions show the pH-dependent trend reported in the literature,[65] this was not the case for the unbuffered solutions (current density vs potential plots are presented in Figure S3). The highest onset potential and lowest photocurrent value are found for the near-neutral solution (Table S1) and not for the neutral solution, as expected. Hence, identical measurements were performed using a bulk three-electrode PEC cell and a higher electrolyte concentration to rule out whether different mass transport conditions or conductivity effects are causing this deviation. CVs measured using 50 and 500 mM unbuffered solutions are shown in Figure S4. However, trends observed in the PEC-ICP-MS measurements were similar to the bulk cell. Since resolving this discrepancy is out of the main scope of this work, we aim to address it in further studies.

To quantify the stability of the Fe_2O_3 electrodes under the OER conditions while recording the CVs, the dissolution was detected in parallel by on-line ICP-MS. The Fe dissolution profiles in buffered and unbuffered electrolytes are displayed in panel III of Figure 2a,2b, respectively. For all studied electrolytes, no dissolution of Fe was detected while collecting the dark CVs, most likely due to Faradaic processes being negligible under these conditions. However, upon irradiation, Fe dissolution is detected in all unbuffered electrolytes. Comparing the extent of Fe dissolution at different pHs, Fe dissolves significantly at alkaline and neutral pH, while dissolution rates are decreased under near-neutral pH conditions. Interestingly, it was reported that Fe dissolution was reduced when the pH of the electrolyte was increased for the Fe_2O_3 + Ir MC system,[29] which is different from the results obtained in this work. The discrepancy might be related to the different performance of the photoanodes used in both studies since the Fe_2O_3 + Ir MC system presented lower photocurrents (up to 0.5 mA cm^{-2} at 1.6 V_{RHE} for the different electrolytes used) or a complex interplay between the Ir molecular catalysts that could affect the photocorrosion mechanism of the Fe_2O_3 photoanode at different pH values. On the other hand, negligible dissolution was observed in all buffered electrolytes. Therefore, it seems that maintaining a
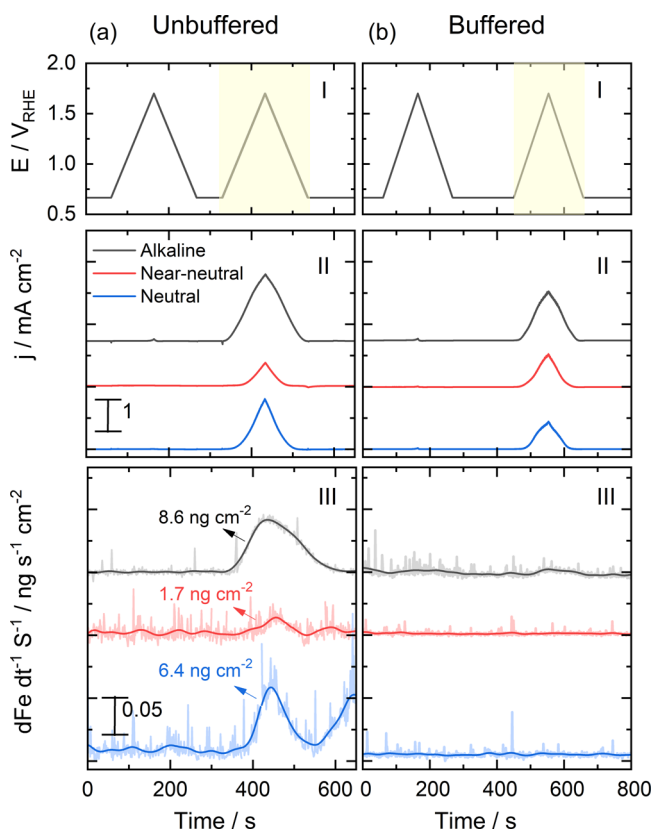

Figure 2. Stability measurement of the Fe_2O_3 nanorods at different pHs during dark and illuminated CVs in (a) unbuffered and (b) buffered electrolytes. Different panels show the (I) potentiostatic protocol vs time, also displaying the illumination period (yellow area); (II) obtained current density; and (III) Fe dissolution detected during the measurement. The obtained raw dissolution results (light color) were smoothed (dark color) by using a FFT filter. The integrated amount of Fe dissolved is indicated for each unbuffered electrolyte.
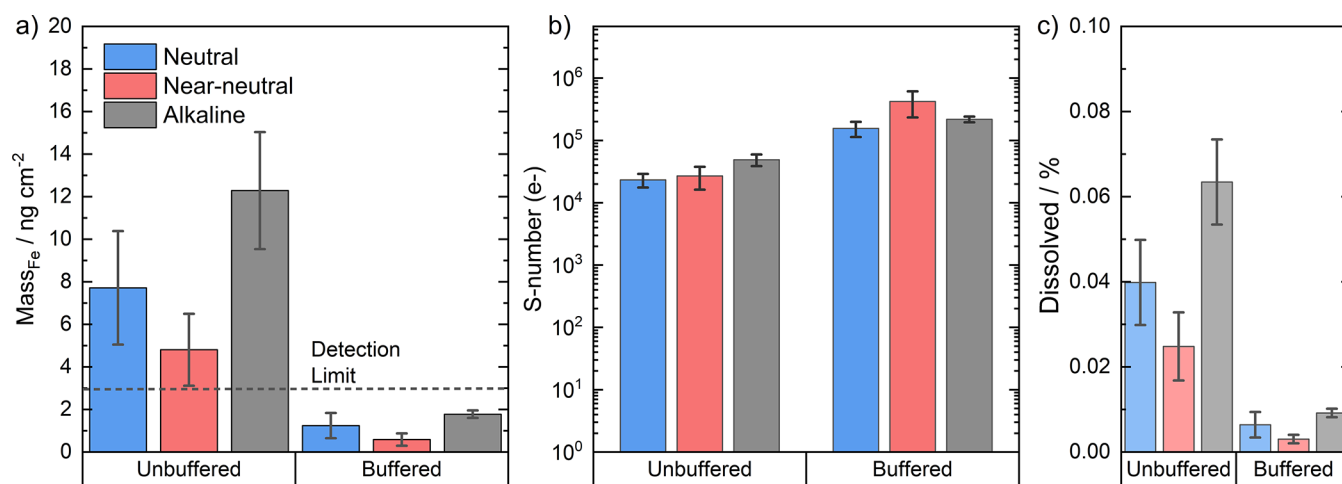
Figure 3. (a) Dissolved amount of Fe during a CA under irradiation for the different electrolytes. The dissolved amount ($mass_{Fe}$) is the average obtained from 2 measurements, and the error bars represent the standard deviation. The dashed line represents the highest Fe detection limit by ICP-MS calculated for the unbuffered near-neutral sample. (b) S-number (e^-) quantified at different pHs in different electrolytes for the Fe_2O_3 nanorods under irradiation. (c) Percentage of the dissolved photoanode during a 10 min CA.

stable local pH (i.e., buffering) remarkably influences the dissolution of Fe_2O_3 photoanodes during irradiation. To see whether the nature of the electrolyte ions (phosphate anions specifically) additionally affects the measured dissolution, further measurements were performed in near-neutral solutions using carbonate buffer at pH 9 (Figure S5). The observed dissolution was also negligible, confirming that the buffered electrolytes notably diminish the photocorrosion of Fe_2O_3 photoanodes, regardless of the anions present in the electrolyte.

Since Sn is present in the substrate and is a dopant of the Fe_2O_3 nanostructures, Sn was also quantified during a dark and irradiated CV (see Figure S6). No dissolution of Sn was observed during this protocol, showing good stability of the substrate and negligible Sn leaching from the Fe_2O_3 nanorods during the experimental conditions used. The results are in accordance to the low percentage of Sn found in Fe_2O_3 and the good stability of FTO films reported up to 2.0 V_{RHE} in the dark.[68]

A second dissolution transient was observed after a CV under irradiation in the neutral electrolyte. This process was further characterized by using additional protocols. First, we confirmed that a transient dissolution is present in unbuffered near-neutral and neutral electrolytes (see Figure S7a) when the potential is shifted back to the OCP after a hold at 1.5 V_{RHE} (CA) under irradiation. Notably, when buffered electrolytes are used, the second transient is also suppressed (Figure S7b), exhibiting a strong effect of buffered electrolytes on the stability of Fe_2O_3 photoanodes again. We observed that holding the potential above the OCP after the CA prevented the transient dissolution from taking place in the unbuffered neutral electrolyte (Figure S7c). This is an important aspect to point out since selecting an appropriate potential upon interruption of irradiation could improve the stability of Fe_2O_3 photoanodes in PEC cells during operation. Furthermore, the cathodic dissolution found could explain the discrepancy with the Fe_2O_3 + Ir MC system,[29] where this transient might have contributed to the higher Fe dissolution observed in the unbuffered near-neutral and neutral electrolytes.

3.3. S-Number (e^-) of the Fe_2O_3 Films in Different Electrolytes and pHs.

Activity and stability are two performance metrics that must be taken into account when choosing optimal PEC materials and operational conditions. As shown above, the measured photocurrent, in conjunction with stability, is highly dependent on the electrolyte and pH solution. To combine activity and stability in one metric, the S-number was defined as the ratio between the evolved oxygen (considering 100% of Faradaic efficiency and neglecting all other processes) and the dissolved amount of catalyst.[69] The former is estimated directly by integrating the measured current density over time and using Faraday's laws of electrolysis, while the latter is obtained from on-line or *ex situ* ICP-MS. In this work, however, we adopt the recently proposed modified S-number (e^-) concept,[40,44] which allows for overcoming the lower than 100% OER Faradaic efficiency limitation, typical in PEC water splitting. Indeed, we cannot ensure that there are no other reactions taking place in the different electrolytes used.[40] The main difference between the S-number and S-number (e^-) is that instead of considering the evolved oxygen, we calculate the amount (in moles) of transferred electrons. To obtain the S-number (e^-), the total mass of Fe dissolved during an irradiated CA (10 min, 1.5 V_{RHE}) was integrated for each electrolyte (see Figure 3a), considering only the dissolution during the CA at 1.5 V_{RHE} (the second dissolution transient was not considered when it was present). Since dissolution was negligible in some cases, we first calculated the detection limit of Fe for all of the electrolytes used (see Table S2). For simplicity, we displayed only the highest detection limit, as shown in Figure 3a, corresponding to the unbuffered near-neutral electrolyte. The mass integrals obtained for the buffered electrolytes are below the nominal detection limit of the ICP-MS instrument. We used these mass integrals to calculate the S-numbers (e^-) for buffered electrolytes, as presented in Figure 3b. However, we should point out that these represent a theoretical approximation, since the real values are certainly higher. Interestingly, the S-numbers (e^-) are on the same order of magnitude for all unbuffered solutions for all studied pHs. When phosphate is used as a buffer, however, an order of magnitude increase in the S-number (e^-) is observed. The results suggest the

following trends: (a) for unbuffered solutions, the stability number does not seem to depend on pH; (b) the presence of buffers clearly decreases the dissolution of Fe_2O_3.
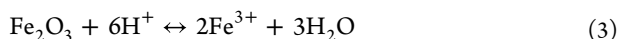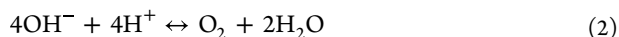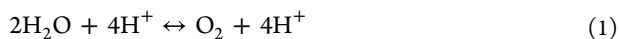
We estimated the percentage of the dissolved film during one irradiated CA, considering the mass per area based on the number of nanorods observed in the SEM, the volume of each nanorod, and the Fe_2O_3 density (5.46 g cm^{-3}).[70] Although the S-number (e$^-$) is in the same order of magnitude for unbuffered electrolytes, the amount dissolved during one CA (Figure 3c) varies in line with the dissolution rates, as observed in Figure 2.

The impact of light intensity on stability was characterized in unbuffered neutral and alkaline electrolytes since higher dissolution rates were observed under these conditions, and the results are presented in Figure S8. We found a linear dependence of dissolution of Fe with the charge passed for the neutral electrolyte, while no linear dependence was observed for the alkaline electrolyte. Since a linear dependence of dissolution with light intensity is associated with a common intermediate between the OER and dissolution, the results might suggest different intermediates during the OER/ dissolution in a near-neutral and alkaline electrolyte. A more detailed discussion is provided in the SI along with Figure S8.

To understand why buffered solutions strongly affect the stability of Fe_2O_3 during irradiation, the different pathways that can lead to Fe_2O_3 photocorrosion should be first considered. The dissolution of Fe during illumination might be ascribed to the following reasons:

(a) corrosion due to a decrease in local pH caused by the OER;[23,29]

(b) self-oxidation of Fe_2O_3 with photogenerated holes.[31]

As mentioned above, the high local concentration of H$^+$ ions formed during the OER could alter the pH in the vicinity of the electrode if unbuffered electrolytes are used. It was proposed in the literature that the protons generated during the OER (eq 1) could accelerate the corrosion of Fe_2O_3 photoanodes in acidic and neutral electrolytes.[23] Also, the consumption of hydroxide ions to evolve molecular oxygen in alkaline media (eq 2) leads to a local decrease in the pH in alkaline electrolytes. An acidic local environment could trigger Fe dissolution, as shown in eq 3.[23]

$$2H_2O + 4H^+ \leftrightarrow O_2 + 4H^+ \tag{1}$$

$$4OH^- + 4H^+ \leftrightarrow O_2 + 2H_2O \tag{2}$$

$$Fe_2O_3 + 6H^+ \leftrightarrow 2Fe^{3+} + 3H_2O \tag{3}$$

The presence of a buffer mitigates the local pH change stemming from the OER and, therefore, decreases dissolution, as can be observed in the results presented in Figure 2. Although the OER was considered responsible for the dissolution of Fe_2O_3 in neutral electrolytes, where local pH can change drastically,[23,29] it is less likely to be the reason behind the dissolution in unbuffered alkaline electrolytes, where higher dissolution rates are observed. For instance, a current density of 0.5 mA cm^{-2} produced a local pH decrease of 2 pH units, which can impact chemical stability when the pH of the electrolyte is 5.[29] However, even when the photocurrent measured in this work is 2 or 3 times higher (up to 1.5 mA cm^{-2}), a pH decrease of 2−3 units would not shift the local pH to a region of chemical instability of Fe_2O_3 (since the starting pH is 13 in the alkaline electrolyte). In

alkaline solutions, the higher OH$^-$ concentration should quickly neutralize the produced protons, or the consumed OH$^-$ would have little impact on the local pH (considering the magnitude of the photocurrents measured under these conditions).

In addition to the local pH, the self-oxidation of Fe_2O_3 can lead to dissolution, according to the following equation:[22]

$$Fe_2O_3 + 6h^+ \leftrightarrow 2Fe^{3+} + 1.5O_2 \tag{4}$$

Equation 4 describes photocorrosion triggered by the reaction with the photogenerated electron vacancies (holes, h$^+$). This leads to the dissolution of Fe (as Fe^{3+} ions) that most likely reacts with water/hydroxide ions to produce $Fe(OH)_3$ or $Fe(OH)_2{}^+$ in neutral, near-neutral, and alkaline electrolytes, according to the Pourbaix diagram.[71,72] Since both photocorrosion pathways depend on the photogenerated holes as an initial reactant, differentiation is challenging, and based on the experimental data obtained in this work, we cannot exclude either self-oxidation or the local pH being responsible for photocorrosion under the conditions used.

Furthermore, the adsorption of the anions could play a key role in the photocorrosion mechanism. Thus, the interaction of the Fe_2O_3 surface with the used electrolyte must be considered.[32,73] It is well reported in the literature that phosphate species can strongly adsorb at Fe_2O_3 surfaces compared to other electrolyte anions (amines, carboxylates, thiols).[74] The use of perchlorate ions is the most ideal from this perspective, since these adsorb at the Fe_2O_3 surface in a nonspecific way.[75] Contrastingly, phosphate ions form inner-sphere complexes at the solid−liquid interface of iron oxides[75,76] that can bridge two iron centers and reinforce the lattice bridging in the surface.[77] It was proposed that these binuclear phosphate complexes retard the reductive and nonreductive chemical dissolution of Fe_2O_3.[78] Therefore, it is indeed possible that the specific adsorption of phosphate ions plays a decisive role in preserving stability.

We demonstrated that PEC-ICP-MS is a useful tool to compare the stability of Fe_2O_3 photoanodes in different electrolytes and at different pH values under irradiation. Fe dissolution has proven to be the highest in unbuffered electrolytes, with the highest dissolution rates at neutral and alkaline pHs, whereas it decreased significantly in buffered electrolytes containing phosphate ions. In this light, we consider that phosphate buffers can improve the stability of Fe_2O_3 either by preventing local acidification in neutral and near-neutral electrolytes (where a local pH decrease can trigger dissolution) due to a buffering effect or by retarding self-oxidation due to the specific adsorption of phosphate anions at the Fe_2O_3 surface.

3.4. Long-Term Measurements of the Fe_2O_3 Films in Different Electrolytes and pHs. Considering these results, phosphate buffers are apparently a better choice for operating Fe_2O_3 photoanodes under irradiation. However, the time scale of our PEC-ICP-MS measurements is very short compared to, for example, an imaginary future industrial application. Unlike other metal oxide photoanodes that show an evident decrease in photocurrent within the first tens of minutes,[41,79] Fe_2O_3 can sustain a steady-state photocurrent for up to a few hours in concentrated neutral[23] and alkaline electrolytes.[80] However, on a longer time scale, other processes can degrade the photoabsorber, such as mechanical erosion due to the OER[81] or surface reconstruction.[82] Therefore, to complement the PEC-ICP-MS results, measurements were performed on a
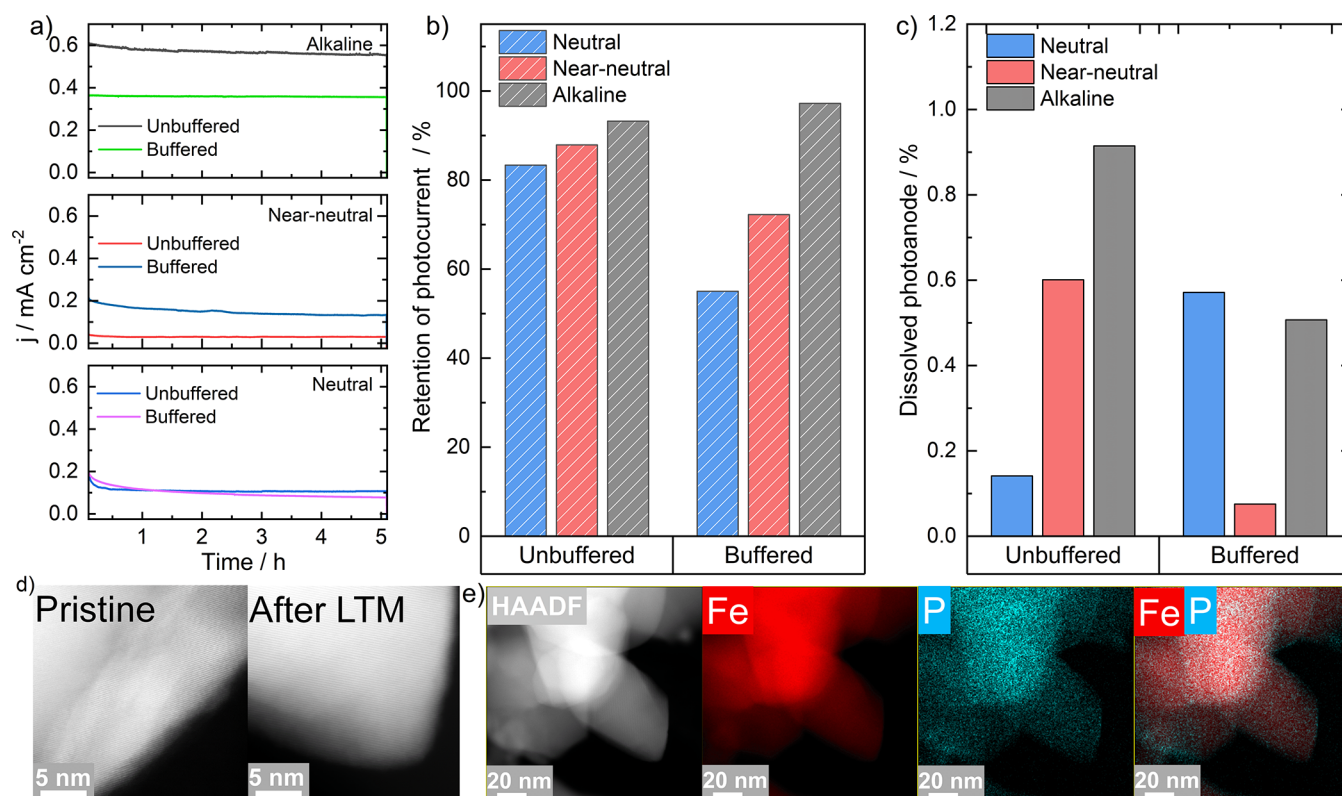
Figure 4. (a) Long-term measurement of the Fe_2O_3 nanorods at different pHs and electrolytes performed in a three-electrode bulk cell. (b) Percentage of photocurrent retained after the long-term measurement for the different unbuffered and buffered electrolytes. (c) Percentage of the film dissolved during the LTM. (d) HR-STEM image of the Fe_2O_3 nanorods. (e) EDX mapping of Fe and P after the long-term measurement in the neutral buffered electrolyte.

longer time scale using the same electrolytes as for the short-term measurements.

A long-term measurement (LTM) of the Fe_2O_3 photo-anodes was performed in unbuffered and buffered solutions, holding the potential at 1.5 V_{RHE} for 5 h in a three-electrode bulk cell under irradiation. Figure 4a summarizes the LTM measurements in different electrolytes. Regarding the performance, a higher photocurrent is observed for the unbuffered alkaline electrolyte and is likely related to the higher pH (13) compared to the that of the buffered alkaline electrolyte (12). Also, a photocurrent enhancement is observed in the buffered near-neutral electrolyte and can be related to the presence of a base that aids the O−H breaking during the OER by accepting protons.[63] As for the performance over time, different trends are found, depending on the pH and electrolyte. A slight decrease in photocurrent is observed over time for the unbuffered alkaline electrolyte, while this is less pronounced in the alkaline buffered electrolyte. An initial decay within the first tens of minutes is observed for the near-neutral and neutral unbuffered electrolytes, but the photocurrent remains relatively stable during the LTM. On the other hand, the buffered neutral and near-neutral electrolytes show a continuous decrease in the photocurrent value during the whole LTM. The change in performance for the different electrolytes during the LTM was considered by measuring the retained photocurrent (the initial photocurrent was taken after 20 min of initiating the CA and the final photocurrent was taken at 5 h). Figure 4b summarizes the percentage of the photocurrent retained for the different electrolytes at different pHs. For both groups of electrolytes, we observe that the

photocurrent is better retained at higher pHs. In the unbuffered alkaline electrolyte, the photocurrent maintained after 5 h is 93%, falling in the ballpark for similar long-term measurements.[83] In comparison to the unbuffered electrolytes, photocurrents drop more drastically for the buffered electrolytes at neutral and near-neutral pH. For instance, the retention is approximately 83% in neutral $NaClO_4$, while it drops to 55% in neutral phosphate buffer. Kim et al. also reported a pronounced decrease in the performance of bare Fe_2O_3 photoanodes in neutral phosphate buffer during a long-term measurement.[23] A CV under irradiation was recorded before and after the LTM to further characterize the change in performance, and the results are plotted in Figure S9. All in all, similar trends were found as in the case of the chronoampero-metric holds.

Finally, the dissolved Fe during the LTM was quantified by *ex situ* ICP-MS. Based on these measurements, the mass percentage of the dissolved photoanode was calculated (Figure 4c). In contrast to the short-term measurements (PEC-ICP-MS), Fe dissolves regardless of the nature of the electrolyte (buffered vs unbuffered). The reason behind this could be the relatively high detection limit of Fe in ICP-MS measurements (Table S2) for the electrolytes used in this work, limiting on-line quantification. On the contrary, the dissolved Fe accumulating in the bulk cell for 5 h was effortlessly quantifiable. Therefore, if we calculate the S-number (e^-) based on the LTM (Figure S10), we observe different trends when compared to the S-number (e^-) obtained from a 10 min CA. First, the S-number (e^-) of the buffered electrolytes decreased since Fe dissolution was detected during the LTM.

On the other hand, the stability decreased for the near-neutral unbuffered electrolyte compared to the other unbuffered electrolytes. This lower stability could be a result of the second dissolution transient observed for the unbuffered, near-neutral electrolyte (see Figure S7). Since we quantified the concentration of Fe after the whole LTM protocol, we could not distinguish between the different dissolution processes, and all dissolution processes contribute to the amount of Fe measured *ex situ*. We performed a 30 min CA hold using the PEC-ICP-MS setup to evaluate if the dissolution detected in the LTM originates from a transient or continuous dissolution (Figure S11). The highest dissolution rate is observed at the beginning of the CA under irradiation for the PEC-ICP-MS protocol. It drops slightly over time but still shows considerable dissolution during the 30 min measurement. This measurement confirms that Fe dissolution is not a transient process. Lastly, considering the results presented in Figure 4b,4c, it is clear that the drop in performance obtained after the LTM does not correlate with the amount of the dissolved photoanode. For instance, the alkaline unbuffered electrolyte maintains the best long-term performance and the highest dissolution over time. Therefore, other surface processes must be responsible for the decrease in the photocurrent of the Fe_2O_3 films during the LTM.

Since we observe a more noticeable decrease in performance in the buffered electrolytes, we hypothesize that phosphate ions might play an active role in degradation, which is different from dissolution, in particular, for neutral and near-neutral pHs. To rule out whether the surface of Fe_2O_3 presents signs of surface reconstruction or degradation, HR-STEM images were captured. For these, the sample after the LTM in the buffered solution at neutral pH was selected since this case represented the highest decrease in performance. The high-resolution STEM images for a pristine sample and a sample taken after the LTM are shown in Figure 4d. No appreciable changes can be observed in terms of morphology on the surface of the nanorods compared to the pristine sample. To scrutinize the possible change in the composition of surface Fe_2O_3, EDXS spectrum imaging of the sample after the LTM was performed. The results are summarized in Figure 4e. The EDXS analysis clearly confirms that phosphorus (P) is present at the surface of the nanorods after the LTM. Although the determined atomic percentage of P related to Fe is only 0.1 at. %, the spectrum image suggests a strong interaction with phosphate anions at the interface leading to a change in surface composition. This was further confirmed by an EDXS line profile along a selected nanostructure (Figure S12). Phosphate buffers are used widely to characterize Fe_2O_3 in neutral media,[22,23,28,35,65,84,85] but so far, little attention has been given to the fact that Fe_2O_3 is prone to react with phosphate anions in a long-term exposition. These results highlight the importance of electrolytes in dictating the stability of electrocatalysts. Earlier, electrolytes were considered only as inert components maintaining conductivity/pH. This picture started to change nowadays since novel experimental results demonstrated that electrolyte components (e.g., cations in alkaline electrolytes) play a key role in determining activity or selectivity.[86,87] Therefore, based on our results, we would like to point out that electrolytes based on phosphate salts can negatively affect the performance of Fe_2O_3 photoanodes when used under PEC conditions at neutral and near-neutral pH.

Our results highlight the importance of comparing dissolution results using different time scales and approaches.

This leads to a broader picture of the degradation processes taking place at the semiconductor−electrolyte interface. Summing up, in short-term measurements using on-line PEC-ICP-MS, we found dissolution of Fe_2O_3 in all unbuffered electrolytes, while such a phenomenon was not detected for buffered electrolytes. In the long term, dissolution was detected in both the unbuffered and buffered electrolytes, regardless of the pH. Additionally, when LTMs were performed, the incorporation of phosphorus in the Fe_2O_3 lattice was detected, further decreasing the activity.

4. CONCLUSIONS

Fe_2O_3 nanorods were prepared using a facile hydrothermal method to successfully reproduce optical, morphological, and PEC properties found in the literature. PEC-ICP-MS measurements revealed that Fe dissolution is triggered by irradiation of the model Fe_2O_3 photoanodes in different unbuffered and buffered solutions at different pHs. Dissolution of Fe was found at all pH values in unbuffered solutions, while the use of buffered electrolytes containing phosphate anions significantly decreased its magnitude, particularly at neutral and near-neutral pH. Longer experiments were performed in a bulk cell, revealing a significant decrease in performance in phosphate-containing electrolytes.

We want to point out that although Fe_2O_3 nanorods are considered extremely stable materials in the literature, our results indicate that dissolution is present at all pHs in unbuffered solutions, even in alkaline electrolytes, in short-term experiments. The presence of a phosphate buffer might prevent dissolution in the short term but lead to more complex processes (e.g., the incorporation of phosphorus in the topmost layer of Fe_2O_3) on a longer time scale, strongly degrading the performance. For example, stable long-term performance could be achieved by depositing thin films based on stable semiconductor oxides such as SnO_2, TiO_2, or Al_2O_3 using atomic layer deposition (ALD) or by covering the Fe_2O_3 nanorods with a cocatalyst such as transition metal-based Co-Pi or NiCoOOH. Our results underline that to harness the immense potential of PEC devices, among others, stability issues must be solved first. The design of stable photoanodes can be only done by deliberately studying process conditions regarding the electrolyte composition, pH, potential window, etc. To realize this goal, several descriptors have to be mapped simultaneously, for which the PEC-ICP-MS setup described in our manuscript will be an invaluable tool.

■ ASSOCIATED CONTENT

ⓢ Supporting Information

The Supporting Information is available free of charge at https://pubs.acs.org/doi/10.1021/acs.jpcc.3c02969.

> Absorption spectrum; onset potentials and photo-currents in different electrolytes; CVs recorded in the bulk cell; stability measurement in a carbonate buffer; stability measurements during a 10 min CA in different electrolytes; Fe detection limit for the different electrolytes used; performance and stability data and discussion under different light intensities in the unbuffered alkaline and neutral electrolytes; CVs before and after the LTM; S-number (e^-) based on LTM measurements; stability measurement using PEC-ICP-MS during 30 min; and EDX mapping (PDF)

■ AUTHOR INFORMATION

Corresponding Authors

Victoria Benavente Llorente − *Forschungszentrum Jülich GmbH, Helmholtz-Institute Erlangen-Nürnberg for Renewable Energy (IEK-11), 91058 Erlangen, Germany;* Present Address: INFIQC−CONICET, Dto. de Fisicoquímica − Facultad de Ciencias Químicas, Universidad Nacional de Córdoba, Ciudad Universitaria, 5000 Córdoba, Argentina; ● orcid.org/0000-0002-9830-7275; Email: victoria.benavente@unc.edu.ar

Attila Kormányos − *University of Szeged, Department of Physical Chemistry and Materials Science, Interdisciplinary Excellence Centre, University of Szeged, Szeged H-6720, Hungary;* ● orcid.org/0000-0002-2145-7419; Email: kormanyos.attila@szte.hu

Serhiy Cherevko − *Forschungszentrum Jülich GmbH, Helmholtz-Institute Erlangen-Nürnberg for Renewable Energy (IEK-11), 91058 Erlangen, Germany;* ● orcid.org/0000-0002-7188-4857; Email: s.cherevko@fz-juelich.de

Authors

Ken J. Jenewein − *Forschungszentrum Jülich GmbH, Helmholtz-Institute Erlangen-Nürnberg for Renewable Energy (IEK-11), 91058 Erlangen, Germany; Department of Chemical and Biological Engineering, Friedrich-Alexander-Universität Erlangen-Nürnberg (FAU), 91058 Erlangen, Germany;* ● orcid.org/0000-0001-8979-7252

Markus Bierling − *Forschungszentrum Jülich GmbH, Helmholtz-Institute Erlangen-Nürnberg for Renewable Energy (IEK-11), 91058 Erlangen, Germany; Department of Chemical and Biological Engineering, Friedrich-Alexander-Universität Erlangen-Nürnberg (FAU), 91058 Erlangen, Germany*

Andreas Körner − *Forschungszentrum Jülich GmbH, Helmholtz-Institute Erlangen-Nürnberg for Renewable Energy (IEK-11), 91058 Erlangen, Germany; Department of Chemical and Biological Engineering, Friedrich-Alexander-Universität Erlangen-Nürnberg (FAU), 91058 Erlangen, Germany*

Andreas Hutzler − *Forschungszentrum Jülich GmbH, Helmholtz-Institute Erlangen-Nürnberg for Renewable Energy (IEK-11), 91058 Erlangen, Germany;* ● orcid.org/0000-0001-5484-707X

Complete contact information is available at:
https://pubs.acs.org/10.1021/acs.jpcc.3c02969

Author Contributions

The manuscript was written through the contributions of all authors. All authors have given approval to the final version of the manuscript.

Notes

The authors declare no competing financial interest.

■ REFERENCES

(1) Nguyen, D. N.; Fadel, M.; Chenevier, P.; Artero, V.; Tran, P. D. Water-Splitting Artificial Leaf Based on a Triple-Junction Silicon Solar Cell: One-Step Fabrication through Photoinduced Deposition of Catalysts and Electrochemical Operando Monitoring. *J. Am. Chem. Soc.* **2022**, *144* (22), 9651−9660.

(2) Wu, H.; Zhang, L.; Du, A.; Irani, R.; van de Krol, R.; Abdi, F. F.; Ng, Y. H. Low-bias photoelectrochemical water splitting via mediating trap states and small polaron hopping. *Nat. Commun.* **2022**, *13* (1), No. 6231.

(3) Segev, G.; Kibsgaard, J.; Hahn, C.; Xu, Z. J.; Cheng, W.-H.; Deutsch, T.; Xiang, C.; Zhang, J. Z.; Hammarstrom, L.; Nocera, D.; et al. The 2022 Solar Fuels Roadmap. *J. Phys. D: Appl. Phys.* **2022**, *55*, No. 323003.

(4) Gibson, E. A. A titanic breakthrough. *Nat. Catal.* **2021**, *4* (9), 740−741.

(5) Choi, M. J.; Kim, T. L.; Choi, K. S.; Sohn, W.; Lee, T. H.; Lee, S. A.; Park, H.; Jeong, S. Y.; Yang, J. W.; Lee, S.; Jang, H. W. Controlled Band Offsets in Ultrathin Hematite for Enhancing the Photo-electrochemical Water Splitting Performance of Heterostructured Photoanodes. *ACS Appl. Mater. Interfaces* **2022**, *14* (6), 7788−7795.

(6) Liu, C.; Zhang, C.; Yin, G.; Zhang, T.; Wang, W.; Ou, G.; Jin, H.; Chen, Z. A Three-Dimensional Branched TiO(2) Photoanode with an Ultrathin Al(2)O(3) Passivation Layer and a NiOOH Cocatalyst toward Photoelectrochemical Water Oxidation. *ACS Appl. Mater. Interfaces* **2021**, *13* (11), 13301−13310.

(7) Maity, D.; Karmakar, K.; Pal, D.; Saha, S.; Khan, G. G.; Mandal, K. One-Dimensional p-ZnCo2O4/n-ZnO Nanoheterojunction Photoanode Enabling Photoelectrochemical Water Splitting. *ACS Appl. Energy Mater.* **2021**, *4* (10), 11599−11608.

(8) Pan, Z.; Nandal, V.; Pihosh, Y.; Higashi, T.; Liu, T.; Röhr, J. A.; Seki, K.; Chu, C.; Domen, K.; Katayama, K. Elucidating the Role of Surface Energetics on Charge Separation during Photoelectrochemical Water Splitting. *ACS Catal.* **2022**, *12* (23), 14727−14734.

(9) Ben-Naim, M.; Britto, R. J.; Aldridge, C. W.; Mow, R.; Steiner, M. A.; Nielander, A. C.; King, L. A.; Friedman, D. J.; Deutsch, T. G.; Young, J. L.; et al. Addressing the Stability Gap in Photo-electrochemistry: Molybdenum Disulfide Protective Catalysts for Tandem III−V Unassisted Solar Water Splitting. *ACS Energy Lett.* **2020**, *5* (8), 2631−2640.

(10) Huang, D.; Li, L.; Wang, K.; Li, Y.; Feng, K.; Jiang, F. Wittichenite semiconductor of Cu(3)BiS(3) films for efficient hydrogen evolution from solar driven photoelectrochemical water splitting. *Nat. Commun.* **2021**, *12* (1), No. 3795.

(11) Zhang, B.; Yu, S.; Dai, Y.; Huang, X.; Chou, L.; Lu, G.; Dong, G.; Bi, Y. Nitrogen-incorporation activates NiFeO(x) catalysts for efficiently boosting oxygen evolution activity and stability of BiVO(4) photoanodes. *Nat. Commun.* **2021**, *12* (1), No. 6969.

(12) Shaner, M. R.; Atwater, H. A.; Lewis, N. S.; McFarland, E. W. A comparative technoeconomic analysis of renewable hydrogen production using solar energy. *Energy Environ. Sci.* **2016**, *9* (7), 2354−2371.

(13) Gerischer, H.; Mindt, W. The mechanisms of the decomposition of semiconductors by electrochemical oxidation and reduction. *Electrochim. Acta* **1968**, *13* (6), 1329−1341.

(14) Gerischer, H. On the stability of semiconductor electrodes against photodecomposition. *J. Electroanal. Chem.* **1977**, *82* (1−2), 133−143.

(15) Gerischer, H. Electrolytic decomposition and photodecomposition of compound semiconductors in contact with electrolytes. *J. Vac. Sci. Technol.* **1978**, *15* (4), 1422−1428.

(16) Barroso, M.; Pendlebury, S. R.; Cowan, A. J.; Durrant, J. R. Charge carrier trapping, recombination and transfer in hematite (α-Fe2O3) water splitting photoanodes. *Chem. Sci.* **2013**, *4* (7), No. 2724.

(17) Mesa, C. A.; Steier, L.; Moss, B.; Francas, L.; Thorne, J. E.; Gratzel, M.; Durrant, J. R. Impact of the Synthesis Route on the Water Oxidation Kinetics of Hematite Photoanodes. *J. Phys. Chem. Lett.* **2020**, *11* (17), 7285−7290.

(18) Subramanian, A.; Gracia-Espino, E.; Annamalai, A.; Lee, H. H.; Lee, S. Y.; Choi, S. H.; Jang, J. S. Effect of tetravalent dopants on hematite nanostructure for enhanced photoelectrochemical water splitting. *Appl. Surf. Sci.* **2018**, *427*, 1203−1212.

(19) Tilley, S. D.; Cornuz, M.; Sivula, K.; Gratzel, M. Light-induced water splitting with hematite: improved nanostructure and iridium oxide catalysis. *Angew. Chem., Int. Ed.* **2010**, *49* (36), 6405−6408.

(20) Li, M.; Yang, Y.; Ling, Y.; Qiu, W.; Wang, F.; Liu, T.; Song, Y.; Liu, X.; Fang, P.; Tong, Y.; Li, Y. Morphology and Doping Engineering of Sn-Doped Hematite Nanowire Photoanodes. *Nano Lett.* **2017**, *17* (4), 2490−2495.

(21) Li, J.; Wan, W.; Triana, C. A.; Chen, H.; Zhao, Y.; Mavrokefalos, C. K.; Patzke, G. R. Reaction kinetics and interplay of two different surface states on hematite photoanodes for water oxidation. *Nat. Commun.* **2021**, *12* (1), No. 255.

(22) Imrich, T.; Krýsová, H.; Neumann-Spallart, M.; Krýsa, J. Fe2O3 photoanodes: Photocorrosion protection by thin SnO2 and TiO2 films. *J. Electroanal. Chem.* **2021**, *892*, No. 115282.

(23) Kim, J. Y.; Jang, J.-W.; Youn, D. H.; Magesh, G.; Lee, J. S. A Stable and Efficient Hematite Photoanode in a Neutral Electrolyte for Solar Water Splitting: Towards Stability Engineering. *Adv. Energy Mater.* **2014**, *4* (13), No. 1400476, DOI: 10.1002/aenm.201400476.

(24) Shen, S.; Zhou, J.; Dong, C. L.; Hu, Y.; Tseng, E. N.; Guo, P.; Guo, L.; Mao, S. S. Surface engineered doping of hematite nanorod arrays for improved photoelectrochemical water splitting. *Sci. Rep.* **2014**, *4*, No. 6627.

(25) Cao, X.; Wang, Y.; Lin, J.; Ding, Y. Ultrathin CoOx nanolayers derived from polyoxometalate for enhanced photoelectrochemical performance of hematite photoanodes. *J. Mater. Chem. A* **2019**, *7* (11), 6294−6303.

(26) Hisatomi, T.; Brillet, J.; Cornuz, M.; Le Formal, F.; Tetreault, N.; Sivula, K.; Gratzel, M. A Ga2O3 underlayer as an isomorphic template for ultrathin hematite films toward efficient photo-electrochemical water splitting. *Faraday Discuss.* **2012**, *155*, 223−232.

(27) Kim, J. Y.; Magesh, G.; Youn, D. H.; Jang, J. W.; Kubota, J.; Domen, K.; Lee, J. S. Single-crystalline, wormlike hematite photo-anodes for efficient solar water splitting. *Sci. Rep* **2013**, *3*, No. 2681.

(28) Klahr, B.; Gimenez, S.; Fabregat-Santiago, F.; Hamann, T.; Bisquert, J. Water oxidation at hematite photoelectrodes: the role of surface states. *J. Am. Chem. Soc.* **2012**, *134* (9), 4294−4302.

(29) Jenewein, K. J.; Wang, Y.; Liu, T.; McDonald, T.; Zlatar, M.; Kulyk, N.; Benavente Llorente, V.; Kormányos, A.; Wang, D.; Cherevko, S. Electrolyte Engineering Stabilizes Photoanodes Deco-rated with Molecular Catalysts. *ChemSusChem* **2023**, *16* (7), No. e202300406.

(30) Krýsa, J.; Němečková, A.; Zlámal, M.; Kotrla, T.; Baudys, M.; Kment, S.; Hubička, Z.; Neumann-Spallart, M. α-Fe2O3/TiO2 stratified photoanodes. *J. Photochem. Photobiol., A* **2018**, *366*, 12−17.

(31) Krýsa, J.; Imrich, T.; Paušová, Š.; Krýsová, H.; Neumann-Spallart, M. Hematite films by aerosol pyrolysis: Influence of substrate and photocorrosion suppression by TiO2 capping. *Catal. Today* **2019**, *335*, 418−422.

(32) Samu, G. F.; Janaky, C. Photocorrosion at Irradiated Perovskite/Electrolyte Interfaces. *J. Am. Chem. Soc.* **2020**, *142* (52), 21595−21614.

(33) Imrich, T.; Zazpe, R.; Krýsová, H.; Paušová, Š.; Dvorak, F.; Rodriguez-Pereira, J.; Michalicka, J.; Man, O.; Macak, J. M.; Neumann-Spallart, M.; Krýsa, J. Protection of hematite photo-electrodes by ALD-TiO2 capping. *J. Photochem. Photobiol., A* **2021**, *409*, No. 113126.

(34) Kennedy, J. H.; Anderman, M. Photoelectrolysis of Water at α-Fe2O3 Electrodes in Acidic Solution. *J. Electrochem. Soc.* **1983**, *130*, 848−852.

(35) Pan, Z.; Yanagi, R.; Higashi, T.; Pihosh, Y.; Hu, S.; Katayama, K. Hematite photoanodes prepared by particle transfer for photo-electrochemical water splitting. *Sustainable Energy Fuels* **2022**, *6* (8), 2067−2074.

(36) Kim, J. H.; Jang, J. W.; Jo, Y. H.; Abdi, F. F.; Lee, Y. H.; van de Krol, R.; Lee, J. S. Hetero-type dual photoanodes for unbiased solar water splitting with extended light harvesting. *Nat. Commun.* **2016**, *7*, No. 13380.

(37) Qu, Y.; Li, F.; Zhang, P.; Zhao, L.; Liu, J.; Song, X.; Gao, L. Enhanced photoelectrochemical performance and stability of Si nanowire photocathode with deposition of hematite and carbon. *Appl. Surf. Sci.* **2019**, *471*, 528−536.

(38) Schrantz, K.; Wyss, P. P.; Ihssen, J.; Toth, R.; Bora, D. K.; Vitol, E. A.; Rozhkova, E. A.; Pieles, U.; Thöny-Meyer, L.; Braun, A. Hematite photoanode co-functionalized with self-assembling melanin and C-phycocyanin for solar water splitting at neutral pH. *Catal. Today* **2017**, *284*, 44−51.

(39) Carminati, S. A.; da Silva, B. L.; Bott-Neto, J. L.; de Melo, M. A.; Galante, M. T.; Fernández, P. S.; Longo, C.; Bonacin, J. A.; Nogueira, A. F. Hematite Nanorods Photoanodes Decorated by Cobalt Hexacyanoferrate: The Role of Mixed Oxidized States on the Enhancement of Photoelectrochemical Performance. *ACS Appl. Energy Mater.* **2020**, *3* (10), 10097−10107.

(40) Knöppel, J.; Kormányos, A.; Mayerhöfer, B.; Hofer, A.; Bierling, M.; Bachmann, J.; Thiele, S.; Cherevko, S. Photocorrosion of WO3 Photoanodes in Different Electrolytes. *ACS Phys. Chem. Au* **2021**, *1* (1), 6−13.

(41) Zhang, S.; Ahmet, I.; Kim, S. H.; Kasian, O.; Mingers, A. M.; Schnell, P.; Kolbach, M.; Lim, J.; Fischer, A.; Mayrhofer, K. J. J.; et al. Different Photostability of BiVO4 in Near-pH-Neutral Electrolytes. *ACS Appl. Energy Mater.* **2020**, *3* (10), 9523−9527.

(42) Zhang, S.; Rohloff, M.; Kasian, O.; Mingers, A. M.; Mayrhofer, K. J. J.; Fischer, A.; Scheu, C.; Cherevko, S. Dissolution of BiVO4 Photoanodes Revealed by Time-Resolved Measurements under Photoelectrochemical Conditions. *J. Phys. Chem. C* **2019**, *123* (38), 23410−23418.

(43) Wilson, H.; Van Rooij, A.; Jenewein, K.; Knöppel, J.; Kormányos, A.; Cherevko, S.; Sunde, S.; Erbe, A. Photocorrosion of n- and p-Type Semiconducting Oxide-Covered Metals: Case Studies of Anodized Titanium and Copper. *Phys. Status Solidi (A)* **2022**, *219*, No. 2100852.

(44) Jenewein, K. J.; Kormányos, A.; Knöppel, J.; Mayrhofer, K. J. J.; Cherevko, S. Accessing In Situ Photocorrosion under Realistic Light Conditions: Photoelectrochemical Scanning Flow Cell Coupled to Online ICP-MS. *ACS Meas. Sci. Au* **2021**, *1* (2), 74−81.

(45) Zhao, L.; Xiao, J.; Huang, H.; Huang, Q.; Zhao, Y.; Li, Y. Enhanced efficiency of hematite photoanode for water splitting with the doping of Ge. *Int. J. Hydrogen Energy* **2018**, *43* (28), 12646−12652.

(46) Sivula, K.; Zboril, R.; Le Formal, F.; Robert, R.; Weidenkaff, A.; Tucek, J.; Frydrych, J.; Grätzel, M. Photoelectrochemical Water Splitting with Mesoporous Hematite Prepared by a Solution-Based Colloidal Approach. *J. Am. Chem. Soc.* **2010**, *132*, 7436−7444.

(47) Makuła, P.; Pacia, M.; Macyk, W. How To Correctly Determine the Band Gap Energy of Modified Semiconductor Photocatalysts Based on UV-Vis Spectra. *J. Phys. Chem. Lett.* **2018**, *9* (23), 6814−6817.

(48) Wang, H.; Turner, J. A. Characterization of Hematite Thin Films for Photoelectrochemical Water Splitting in a Dual Photo-electrode Device. *J. Electrochem. Soc.* **2010**, *157* (11), No. F173, DOI: 10.1149/1.3489940.

(49) Sivula, K.; Le Formal, F.; Gratzel, M. Solar water splitting: progress using hematite (alpha-Fe(2) O(3)) photoelectrodes. *ChemSusChem* **2011**, *4* (4), 432−449.

(50) Patra, A. K.; Kundu, S. K.; Bhaumik, A.; Kim, D. Morphology evolution of single-crystalline hematite nanocrystals: magnetically recoverable nanocatalysts for enhanced facet-driven photoredox activity. *Nanoscale* **2016**, *8* (1), 365−377.

(51) Qiu, P.; Yang, H.; Yang, L.; Wang, Q.; Ge, L. Solar water splitting with nanostructured hematite: The role of annealing-temperature. *Electrochim. Acta* **2018**, *266*, 431−440.

(52) Bassi, P. S.; Xianglin, L.; Fang, Y.; Loo, J. S.; Barber, J.; Wong, L. H. Understanding charge transport in non-doped pristine and surface passivated hematite (Fe2O3) nanorods under front and

backside illumination in the context of light induced water splitting. *Phys. Chem. Chem. Phys.* **2016**, *18* (44), 30370−30378.

(53) Annamalai, A.; Subramanian, A.; Kang, U.; Park, H.; Choi, S. H.; Jang, J. S. Activation of Hematite Photoanodes for Solar Water Splitting: Effect of FTO Deformation. *J. Phys. Chem. C* **2015**, *119* (7), 3810−3817.

(54) Ling, Y.; Wang, G.; Wheeler, D. A.; Zhang, J. Z.; Li, Y. Sn-doped hematite nanostructures for photoelectrochemical water splitting. *Nano Lett.* **2011**, *11* (5), 2119−2125.

(55) Wang, Y.; Rong, M.; Zheng, J.; Rui, Z. Morphology control of the hematite photoanodes for photoelectrochemical water splitting. *Int. J. Hydrogen Energy* **2020**, *45* (56), 31667−31677.

(56) Chai, H.; Gao, L.; Jin, J. Revealing the Essential Role of Iron Phosphide and its Surface-Evolved Species in the Photoelectrochemical Water Oxidation by Gd-Doped Hematite Photoanode. *ChemSusChem* **2022**, *15* (17), No. e202201030.

(57) Wang, L.; Zhu, J.; Liu, X. Oxygen-Vacancy-Dominated Cocatalyst/Hematite Interface for Boosting Solar Water Splitting. *ACS Appl. Mater. Interfaces* **2019**, *11* (25), 22272−22277.

(58) Dworschak, D.; Brunnhofer, C.; Valtiner, M. Photocorrosion of ZnO Single Crystals during Electrochemical Water Splitting. *ACS Appl. Mater. Interfaces* **2020**, *12* (46), 51530−51536.

(59) Knöppel, J.; Zhang, S.; Speck, F. D.; Mayrhofer, K. J. J.; Scheu, C.; Cherevko, S. Time-resolved analysis of dissolution phenomena in photoelectrochemistry − A case study of WO3 photocorrosion. *Electrochem. Commun.* **2018**, *96*, 53−56.

(60) Wilson, H.; Van Rooij, A.; Jenewein, K.; Knöppel, J.; Kormányos, A.; Cherevko, S.; Sunde, S.; Erbe, A. Photocorrosion of n- and p-Type Semiconducting Oxide-Covered Metals: Case Studies of Anodized Titanium and Copper. *Phys. Status Solidi (A)* **2022**, *219*, No. 2100852, DOI: 10.1002/pssa.202100852.

(61) Jenewein, K. J.; Thienhaus, S.; Kormányos, A.; Ludwig, A.; Cherevko, S. High-throughput exploration of activity and stability for identifying photoelectrochemical water splitting materials. *Chem. Sci.* **2022**, *13* (46), 13774−13781.

(62) Iandolo, B.; Hellman, A. The role of surface States in the oxygen evolution reaction on hematite. *Angew. Chem., Int. Ed.* **2014**, *53* (49), 13404−13408.

(63) Zhang, Y.; Zhang, H.; Ji, H.; Ma, W.; Chen, C.; Zhao, J. Pivotal Role and Regulation of Proton Transfer in Water Oxidation on Hematite Photoanodes. *J. Am. Chem. Soc.* **2016**, *138* (8), 2705−2711.

(64) Zhang, Y.; Zhang, H.; Liu, A.; Chen, C.; Song, W.; Zhao, J. Rate-Limiting O-O Bond Formation Pathways for Water Oxidation on Hematite Photoanode. *J. Am. Chem. Soc.* **2018**, *140* (9), 3264−3269.

(65) Liu, Y.; Le Formal, F.; Boudoire, F.; Guijarro, N. Hematite Photoanodes for Solar Water Splitting: A Detailed Spectroelectrochemical Analysis on the pH-Dependent Performance. *ACS Appl. Energy Mater.* **2019**, *2* (9), 6825−6833.

(66) Chatman, S.; Zarzycki, P.; Preocanin, T.; Rosso, K. M. Effect of surface site interactions on potentiometric titration of hematite (alpha-Fe2O3) crystal faces. *J. Colloid Interface Sci.* **2013**, *391*, 125−134.

(67) Lützenkirchen, J.; Preočanin, T.; Stipić, F.; Heberling, F.; Rosenqvist, J.; Kallay, N. Surface potential at the hematite (001) crystal plane in aqueous environments and the effects of prolonged aging in water. *Geochim. Cosmochim. Acta* **2013**, *120*, 479−486.

(68) Geiger, S.; Kasian, O.; Mingers, A. M.; Mayrhofer, K. J. J.; Cherevko, S. Stability limits of tin-based electrocatalyst supports. *Sci. Rep.* **2017**, *7* (1), No. 4595.

(69) Geiger, S.; Kasian, O.; Ledendecker, M.; Pizzutilo, E.; Mingers, A. M.; Fu, W. T.; Diaz-Morales, O.; Li, Z.; Oellers, T.; Fruchter, L.; et al. The stability number as a metric for electrocatalyst stability benchmarking. *Nat. Catal.* **2018**, *1* (7), 508−515.

(70) Boumaza, S.; Boudjemaa, A.; Omeiri, S.; Bouarab, R.; Bouguelia, A.; Trari, M. Physical and photoelectrochemical characterizations of hematite α-Fe2O3: Application to photocatalytic oxygen evolution. *Sol. Energy* **2010**, *84* (4), 715−721.

(71) Scaife, D. E. Oxide semiconductors in photoelectrochemical conversion of solar energy. *Sol. Energy* **1980**, *25* (1), 41−54.

(72) Pourbaix, M. *Atlas of Electrochemical Equilibria in Aqueous Solutions*; Pergamon Press Ltd., 1974.

(73) Nandjou, F.; Haussener, S. Kinetic Competition between Water-Splitting and Photocorrosion Reactions in Photoelectrochemical Devices. *ChemSusChem* **2019**, *12* (9), 1984−1994.

(74) Blanck, S.; Marti, C.; Loehle, S.; Steinmann, S. N.; Michel, C. (Dis)Similarities of adsorption of diverse functional groups over alumina and hematite depending on the surface state. *J. Chem. Phys.* **2021**, *154* (8), No. 084701.

(75) Moss, R. E.; Pérez-Roa, R. E.; Anderson, M. A. Effects of pH on Phosphate Adsorption to Hematite as Studied with Cyclic Voltammetry and Electrochemical Impedance Spectroscopy. *J. Electrochem. Soc.* **2013**, *160* (2), H105−H112.

(76) Huang, X.; Foster, G. D.; Honeychuck, R. V.; Schreifels, J. A. The maximum of phosphate adsorption at pH 4.0: why it appears on aluminum oxides but not on iron oxides. *Langmuir* **2009**, *25* (8), 4450−4461.

(77) Elzinga, E. J.; Sparks, D. L. Phosphate adsorption onto hematite: an in situ ATR-FTIR investigation of the effects of pH and loading level on the mode of phosphate surface complexation. *J. Colloid Interface Sci.* **2007**, *308* (1), 53−70.

(78) Biber, M. V.; dos Santos Afonso, M.; Stumm, W. The coordination chemistry of weathering: IV. Inhibition of the dissolution of oxide minerals. *Geochim. Cosmochim. Acta* **1994**, *58*, 1999−2010.

(79) Schnell, P.; Cruz, J. M. C. M. D.; Kölbach, M.; van de Krol, R.; Abdi, F. F. pH-Dependent Stability of α-SnWO4 Photoelectrodes. *Chem. Mater.* **2022**, *34* (4), 1590−1598.

(80) Yu, Q.; Meng, X.; Wang, T.; Li, P.; Ye, J. Hematite Films Decorated with Nanostructured Ferric Oxyhydroxide as Photoanodes for Efficient and Stable Photoelectrochemical Water Splitting. *Adv. Funct. Mater.* **2015**, *25* (18), 2686−2692.

(81) Dias, P.; Vilanova, A.; Lopes, T.; Andrade, L.; Mendes, A. Extremely stable bare hematite photoanode for solar water splitting. *Nano Energy* **2016**, *23*, 70−79.

(82) Xie, J.; Yang, P.; Liang, X.; Xiong, J. Self-Improvement of Ti:Fe2O3 Photoanodes: Photoelectrocatalysis Improvement after Long-Term Stability Testing in Alkaline Electrolyte. *ACS Appl. Energy Mater.* **2018**, *1* (6), 2769−2775.

(83) Kong, H.; Park, J. S.; Kim, J. H.; Hwang, S.; Yeo, J. Hydrothermal Synthesis in Gap: Conformal Deposition of Textured Hematite Thin Films for Efficient Photoelectrochemical Water Splitting. *ACS Appl. Mater. Interfaces* **2022**, *14* (14), 16515−16526.

(84) Chen, L.; Yang, X.; Chen, J.; Liu, J.; Wu, H.; Zhan, H.; Liang, C.; Wu, M. Continuous shape- and spectroscopy-tuning of hematite nanocrystals. *Inorg. Chem.* **2010**, *49* (18), 8411−8420.

(85) Chong, R.; Wang, B.; Su, C.; Li, D.; Mao, L.; Chang, Z.; Zhang, L. Dual-functional CoAl layered double hydroxide decorated α-Fe2O3 as an efficient and stable photoanode for photoelectrochemical water oxidation in neutral electrolyte. *J. Mater. Chem. A* **2017**, *5* (18), 8583−8590.

(86) Garcia, A. C.; Touzalin, T.; Nieuwland, C.; Perini, N.; Koper, M. T. M. Enhancement of Oxygen Evolution Activity of Nickel Oxyhydroxide by Electrolyte Alkali Cations. *Angew. Chem., Int. Ed.* **2019**, *58* (37), 12999−13003.

(87) Marcandalli, G.; Monteiro, M. C. O.; Goyal, A.; Koper, M. T. M. Electrolyte Effects on CO(2) Electrochemical Reduction to CO. *Acc. Chem. Res.* **2022**, *55* (14), 1900−1911.